Acta Biomaterialia 101 (2020) 575–585

Contents lists available at ScienceDirect

Acta Biomaterialia

journal homepage: www.elsevier.com/locate/actbio

Full length article

Local intragranular misorientation accelerates corrosion in biodegradable Mg

Wenhui Wang[a], Hongliu Wu[a], Yu Sun[a], Jun Yan[b], Lei Zhang[c], Shaoxiang Zhang[c,*], Jiahua Ni[d,*], Yang Song[e,*], Xiaonong Zhang[a,*]

[a] State Key Laboratory of Metal Matrix Composites, School of Materials Science and Engineering, Shanghai Jiao Tong University, Shanghai 200240, China
[b] Department of General Surgery, Shanghai Jiao Tong University Affiliated Sixth People's Hospital, Shanghai 200233, China
[c] Suzhou Origin Medical Technology Co. Ltd., Jiangsu 215513, China
[d] John A. Paulson School of Engineering and Applied Sciences, Harvard University, 29 Oxford Street, Cambridge, MA 02138, USA
[e] Department of Biomedical Engineering, Georgia Institute of Technology, Atlanta 30332, USA

ARTICLE INFO

Article history:
Received 8 August 2019
Revised 27 September 2019
Accepted 24 October 2019
Available online 28 October 2019

Keywords:
Mg
Corrosion
Microstructure
Local misorientation
Grain boundary (GB)

ABSTRACT

Mg-based implants are used in biomedical applications predominantly because of their degradable property. In this paper, the effect of local misorientations (intragranular misorientation) on the corrosion behavior of high-purity Mg (HPM) was systematically investigated according to microstructure characterization and corrosion measurements. The results showed that local misorientation introduced into grains by deformation could result in corrosion around the grain boundary (GB), which ultimately reduces the corrosion resistance of HPM. After removing the local misorientation by annealing, the corrosion around GB could be eliminated. This work is expected to inspire better control over the degradation behaviors of biomedical Mg through microstructure design to be used for various biomedical applications.

Statement of significance

1. Fine grains, fine grains with large local misorientation, and coarse grains could be obtained, respectively, in high-purity Mg by sequential hot rolling, compression deformation, and annealing treatments.
2. Large local misorientation introduced into grains could lead to corrosion around the grain boundary and ultimately reduce corrosion resistance.
3. In the absence of local misorientation, refining grain size could improve the corrosion resistance of Mg.

1. Introduction

Biodegradable metals including Mg, Zn, and Fe are receiving increasing attention because of the imperative clinical demands for temporary implantation [1–6]. Among them, Mg has been proven to have bio-functions such as good cytocompatibility, antibacterial properties, and superior performance of osseointegration [7–13]. On the basis of the results of research on high-purity Mg [13–15], many kinds of novel Mg-based implants such as cardiovascular stent, bone screw, and vascular clip have entered clinical trials [16–18]. Nevertheless, the fast degradation rate of the Mg implant, which can largely affect its mechanical performance and biocompatibility, is still a bottleneck for restraining their application [19,20]. For example, formation of gas cavities around the Mg implant and fracture caused by the fast decay of strength has been reported in the past [16]. Therefore, achieving control over the corrosion resistance of biodegradable Mg remains a crucial challenge for its biomedical applications.

In addition to external environmental factors, the corrosion resistance of Mg can also be influenced by its intrinsic microstructural features such as grain boundary (GB) [21–23], precipitates [24–26], grain orientation [27–30], solute atom [31–33], and dislocation [34]. Presently, most biodegradable Mg alloys are the wrought alloys, which exhibit much better mechanical properties than the cast alloys, because of the fine-grained strengthening effect produced by plastic deformation [35,36]. Moreover, many researchers have also confirmed that the corrosion resistance of Mg could be improved with the decrease in grain size (increase in the density of GB), which generates a more stable corrosion product

* Corresponding authors.
E-mail addresses: sxzhang@originmedtech.com (S. Zhang), jiahua.ni@sjtu.edu.cn (J. Ni), ysong65@gatech.edu (Y. Song), xnzhang@sjtu.edu.cn (X. Zhang).

https://doi.org/10.1016/j.actbio.2019.10.036
1742-7061/

Table 1
Chemical compositions of HPM as analyzed by ICP-AES.

Element	Mg	Si	Fe	Ni	Cu	Al	Mn	Ti	Pb	Sn	Zn
ppmw	Bal.	20	20	5	5	20	20	10	10	5	20

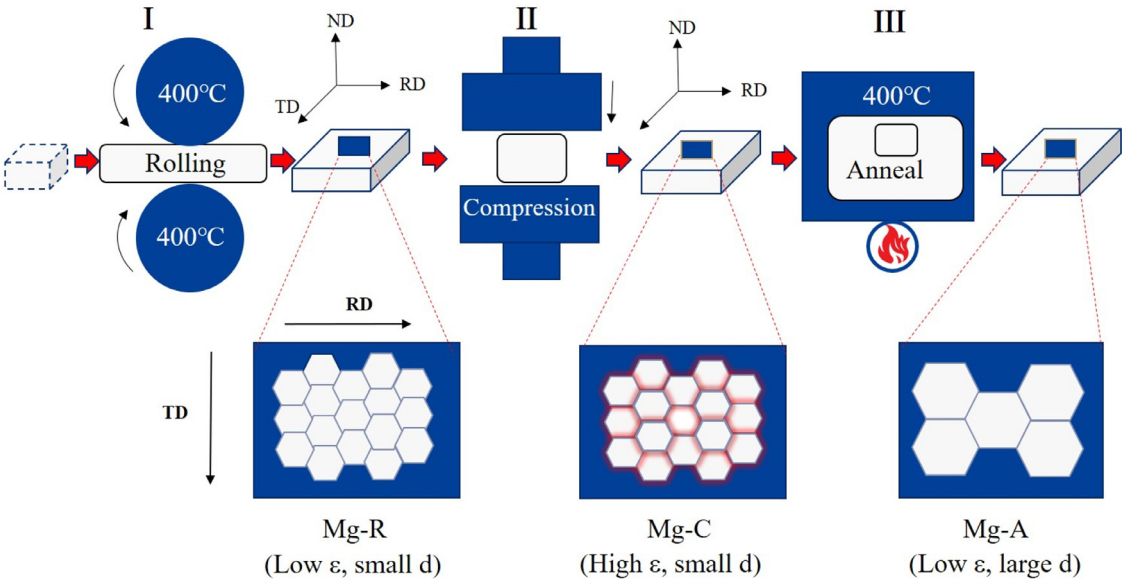

Fig. 1. Mechanical processing and heat treatment of high-purity magnesium (HPM) to obtain grains with different residual strain (ε) and size (d).

layer [37–41]. Here, GB is actually a misorientation between two adjacent grains with different crystal orientation (this misorientation is also called GB misorientation). However, there are also some intragranular misorientations, that is, the local misorientation within the grain. The local misorientation within the grain is normally less stable and contains higher residual stress/strain than that in GB. Unfortunately, thus far, only few studies have focused on the effect of local misorientation on the corrosion of Mg. The strain-induced grain refinement of Mg also produces local misorientation after plastic deformation, which may have an important influence on the corrosion resistance [42]. For example, Song et al. reported that the corrosion resistance of pure Mg and AZ91D decreased in the case of significant reduction in grain size after mechanical processing [43,44]. Other researchers have also reported that the corrosion current increased with increase in the strain during tensile and compression deformation processes [34,45]. In these studies, the local misorientation is prone to be produced by plastic deformation. Therefore, the effect of local misorientation on the corrosion behavior of biodegradable Mg should be considered, which can potentially provide information for wrought Mg alloy.

Thus, we have attempted to reveal the effect of local misorientation on the corrosion behavior of Mg and want to gain attention of other researchers about this work. Because of the geometrically necessary dislocations (GNDs) formed in the material after plastic deformation, the residual strain was stored as local variations in lattice orientation [46]. Hence, local misorientation and strain distribution could be characterized by electron backscatter diffraction (EBSD) [47]. Here, a high level of local misorientation (misorientation angle 0.5°–3°) was produced in HPM through compression deformation at room temperature. The corrosion behavior of compressive HPM was studied using electrochemical and immersion measurements, and then it was also compared with that of an original hot rolling sample and an annealed sample. The distribution of local misorientation and the corroded micro-morphology of all samples were characterized ex situ, respectively, to directly reveal the relationship between local misorientation and corrosion behavior. We found that both the content and the distribution of local misorientation have high influence on corrosion. The main mechanism is that the region with large local misorientation contains the high stored energy and residual stress, which can increase the dissolution rate of the Mg substrate. These findings can assist us to better understand the relationship between the microstructure and the degradation behavior of biomedical Mg from the perspective of materials.

Table 2
Strength, modulus, and hardness of HPM sheets.

	YS/UTS (MPa)	Modulus (GPa)	Hardness (HV)
Mg-R	105/142	45	42.3
Mg-C	118/157	45	46.7
Mg-A	73/108	45	37.6

2. Materials and methods

2.1. Material processing

The as-casted ingots of Mg with a high purity of 99.98% were selected for research, provided by Suzhou Origin Medical Technology Co. Ltd., China. The chemical compositions of HPM were analyzed using a plasma-atomic emission spectrometer (ICP-AES), and the results are listed in Table 1. As shown in Fig. 1, first, a rectangular plate of size 50 (RD) × 50 (TD) × 30 (ND) mm^3 was cut from the ingot for hot rolling at 400 °C, and then the resultant sample with a total rolling thickness reduction of 80% through eight passes was named as Mg-R. Following the rolling plane of the sheet, Mg-R compressed by a strain of 5% at room temperature was named as Mg-C. Finally, after further annealing at 400 °C for 1 h, the resulting sample was named as Mg-A. The strength, modulus, and hardness of these samples are shown in Table 2.

2.2. Microstructural analysis

The microstructure features including GB, grain orientation, texture, and residual strain were characterized by EBSD measurements performed with a scanning electron microscope (Mira3 (SEM) & AZtec Nordlys Max3 (EBSD)). The data of EBSD results were analyzed using Channel 5 analysis software. Specimens for EBSD measurements were prepared by conventional grinding and diamond polishing (down to 0.5 μm), followed by Ar^+ ion milling in a precision ion polishing system (PIPS, Gatan). The accelerating voltage in operation was 0.5 kV, and the incident angle was set at 3° under a liquid nitrogen cooling system. The morphology of the corroded surfaces after 30 min and 168 h immersion without corrosion products was studied by scanning electron microscopy in the secondary electron mode. For transmission electron microscopy (TEM) analysis, thin foil specimens were prepared by punching 3 mm diameter discs, followed by dimple grinding and Ar^+ ion milling in a precision ion polishing system. The accelerating voltage in operation was 4.5 kV, and the incident angle was set at 6°. TEM operation was performed in a FEI Talos-F200X (200 kV) equipped with a field-emission gun. The Super-EDS X-ray detection system combined with the high current density electron beam in the scanning mode (STEM) was also utilized to analyze the corrosion morphology.

2.3. Corrosion resistance testing

Electrochemical corrosion tests were performed using the PARSTAT 2273 electrochemical system in a simulated body fluid solution (m-SBF [48]) with a pH value of 7.4 at 37 °C. A conventional three-electrode system was used in our tests. The specimen, a platinum electrode, and a saturated calomel electrode (SCE) served as the working electrode, counter electrode, and reference electrode, respectively. The specimen was cold mounted using epoxy resin, with an exposed surface area of 0.5 cm^2. Electrochemical impedance spectroscopy (EIS) measurements were taken at open circuit over a frequency ranging from 100 kHz to 0.01 Hz after 1 h of stabilization at the open-circuit potential (OCP). The amplitude of the applied perturbation was 5 mV. Potentiodynamic polarization tests were performed by applying a potential from OCP

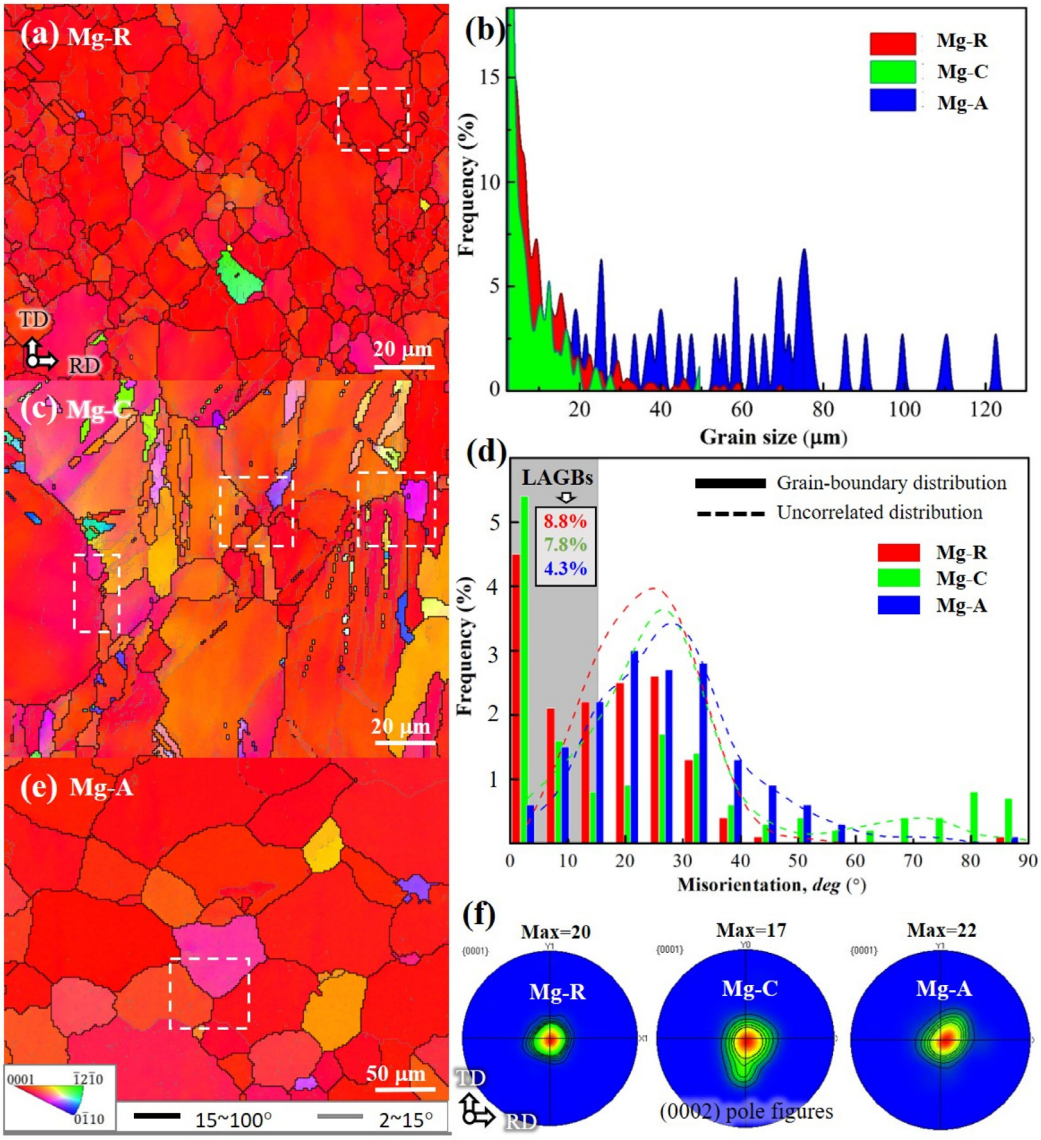

Fig. 2. EBSD inverse pole figure maps of Mg-R (a), Mg-C (c), and Mg-A (e) (the color map representing the grain orientation of each sample is indicated in the inserted crystallographic axes); (b) the distribution of grain size; (d) the distribution of grain boundary misorientation; (f) (0002) pole figures. (For interpretation of the references to color in this figure legend, the reader is referred to the web version of this article.)

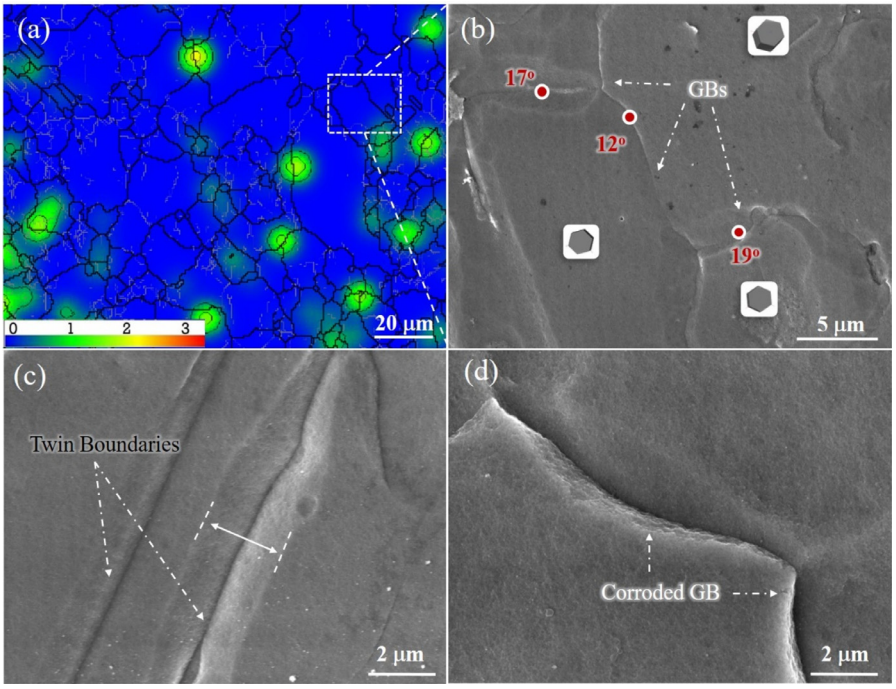

Fig. 3. Local misorientation maps (0°–3°) and the corrosion morphology of Mg-R with 30 min immersion in m-SBF at 37 °C. (a) KAM maps of EBSD-containing grains showing the distribution of local misorientation (For the indexed areas, a higher degree of micro-strain is seen in the area with brighter green color.); (b–d) SEM (secondary electron mode) images of corrosion morphology without corrosion products (selected high-angle GBs are marked (b)). (For interpretation of the references to color in this figure legend, the reader is referred to the web version of this article.)

−500 mV to +500 mV at a scan rate of 2 mV/s, respectively. The immersion test, which can measure continuous hydrogen evolution and the weight loss of the sample, lasted for 168 h in m-SBF at 37 °C. The ratio of the m-SBF solution (ml) to the volume of the sample surface area (cm^2) was 200 ml/cm^2. Before weighing, the corroded sample was cleaned by washing with 180 g L^{-1} CrO_3 solution.

2.4. Statistical methods

The values (mean values, standard deviation) determined in the present study were calculated using Microsoft Excel 2016 software (Microsoft Office, Microsoft Corporation, USA). Statistical analysis was performed with SPSS (SPSS 16.0 Inc., Chicago, USA). One-way ANOVA and Student–Newman–Keuls post hoc tests were used to determine the level of significance. p values less than 0.05 were considered to be significant.

3. Experimental results

3.1. Microstructural characterization

The microstructure of HPM with different processing is demonstrated in Fig. 2 (Mg–R (Fig. 2(a)), Mg–C (Fig. 2(c)), and Mg–A (Fig. 2(e)). After hot rolling at 400 °C, the Mg–R shows a microstructure of dynamical recrystallization, but the grain size is not homogeneous as shown in Fig. 2(a). The average grain size of Mg–R is approximately 11.6 μm. The grains of Mg–C are deformed, and the average size is approximately 14.2 μm after compression at room temperature. The distribution of grain size and the GB misorientation of Mg–R and Mg–C are still similar (Fig. 2(b) and (d)). In addition, the content of low-angle grain boundaries (LAGBs) has also not changed too much: 8.8% and 7.8% in Mg–R and Mg–C, respectively. After annealing treatment at 400 °C for 1 h, the microstructure of the resulting Mg-A has changed and the average grain size increases rapidly to approximately 71.2 μm because of static recrystallization as shown in Fig. 2(e). All three samples exhibit a similar basal texture as shown in Fig. 2(f). The grains are mainly oriented to (0001) and the maximum intensity of texture is 20, 17, and 22 for HPM-R, Mg-C, and Mg-A, respectively, indicating that the c-axis of the grains is nearly perpendicular to the rolled surface. The magnified corrosion morphology of the rectangle regions in Fig. 2(a), (c), and (e) is exhibited in the subsequent part.

To determine the different corrosion behavior caused by microstructural factors in the three HPM samples, we examined GBs, local misorientation, and early corrosion morphology (30 min immersion in m-SBF solution at 37 °C) of the corroded surface without corrosion products by combining EBSD and SEM. By using EBSD, the local misorientation can be expressed by kernel average misorientation (KAM) parameters. The KAM parameter is delineated as that for a given data point, and the average misorientation between the data point and all of its neighbors is calculated [46,47]. The white areas in the KAM map, which are the nonindexed regions, represent the greatest lattice distortion, implying a higher level of residual strain. Although the dynamic recrystallization effect occurs during hot processing, some grains in HPM-R still have more or less local misorientation as shown in Fig. 3(a). The local misorientation has sparse distribution and at a low level. Most of them are located around GBs. From the initial corrosion morphology of Mg-R, we can observe the different corrosion around GBs as shown in Fig. 3(b)–(d). Some GBs have a corrosion gap (Fig. 3(b)), while some GBs are only slightly corroded. In addition, the twin boundaries of Mg-R also have a prior corrosion, but the corrosion of two boundaries is not the same (Fig. 3(c)). One is with a typical width of 1–2 μm, and another just looks like a corroded line. On the basis of these results of the Mg-R sample, if just considering the grain orientation, then the difference in cor-

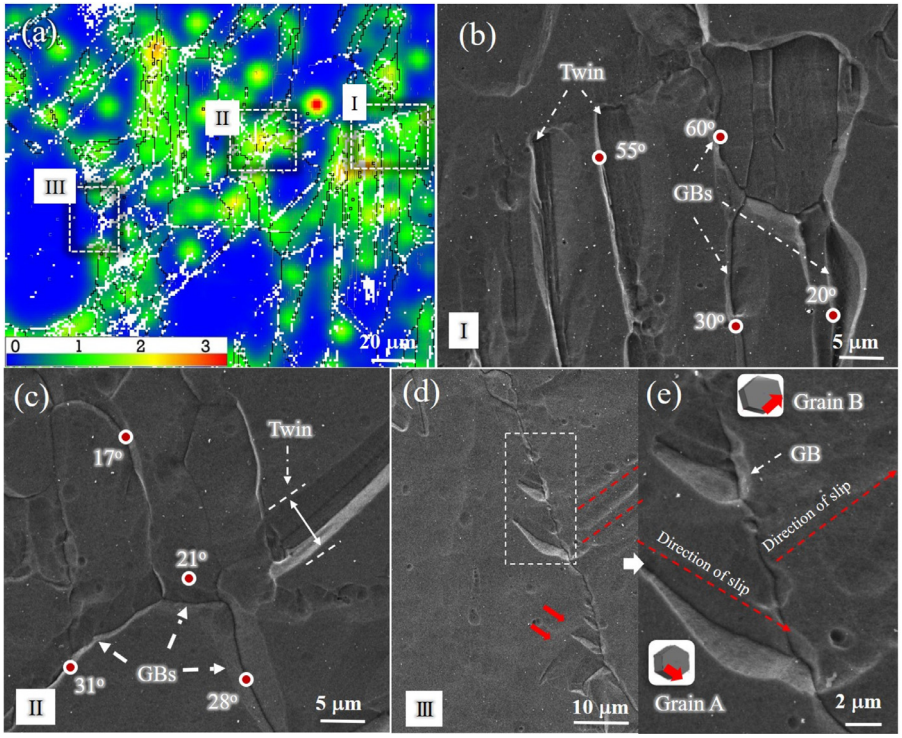

Fig. 4. Local misorientation maps (0°–3°) and the corrosion morphology of Mg-C with 30 min immersion in m-SBF at 37 °C. (a) KAM maps of EBSD-containing grains showing the distribution of local misorientation. The nonindexed regions have the highest local strain; (b–e) SEM (secondary electron mode) images of corrosion morphology without corrosion products (selected high-angle GBs are marked (b, c)).

rosion morphology around GBs seems likely to be caused by low-angle GBs because low-angle GB has a better corrosion resistance than high-angle GB [49].

The local misorientation in Mg-C is much higher than that in Mg-R as shown in Fig. 4, and it is enriched around GBs to some extent. We can observe severe localized corrosion around the GBs despite a low-angle or a high-angle boundary after 30 min of immersion in m-SBF at 37 °C as shown in Fig. 4(b)–(d), although a high-angle boundary is supposed to corrode faster because of the higher interface energy [50]. This result of Mg-C indicates a stronger correlation between local misorientation and corrosion, as these regions of prior corrosion (Fig. 4(b)–(d)) are almost the same as the distribution of local misorientation (Fig. 4(a)). In addition, as shown in Fig. 3(b) and (c), the twins in Mg-R are totally corroded because of the large residual strain caused by deformation. Fig. 4(d) and (e) further shows that the serious corrosion damage propagates along the direction of slip band, resulting in serration-shaped corrosion morphology on both sides of a GB (Fig. 4(d)). Accordingly, local misorientation within grains can lead to a higher corrosion rate, and the GB corrosion should be caused by the large residual strain with the high level of local misorientation.

To further consider the effect of residual strain on corrosion, we removed the local misorientation through annealing treatment to observe the corrosion characteristics. As shown in Fig. 5(a), Mg-A has less local misorientation attributed to the recrystallization of grains during the annealing treatment. More uniform corroded surface is observed in Mg-A after the same immersion test as shown in Fig. 5(b). As the local misorientation almost diminishes, corrosion at the GB indeed becomes trivial regardless (Fig. 5(c)). The GBs can be distinguished only depending on the difference in the corrosion morphology of two grains in some regions as shown in Fig. 5(d). Therefore, the corrosion behavior around GBs without local misorientation is similar to that in the inner grain of HPM, comparing results from Figs. 4 and 5.

The corrosion morphologies of these samples are shown in Fig. 6 to reveal the corrosion propagations after 7 days of immersion. The corroded surface of Mg-R (Fig. 6(a)) and Mg-A (Fig. 6(c)) remains uniform corrosion relative to that in Mg-C (Fig. 6(b)). Again, Mg-C with the largest residual strain has localized attack. Its corroded surface is very inhomogeneous as shown in Fig. 6(b). Comparing Mg-R and Mg-C, a dim GB starts to appear on the surface of Mg-A, suggesting the grain orientation has limited impact on the corrosion rate in the absence of local misorientation [51,52].

3.2. Corrosion measurement

The corrosion resistance of these samples was evaluated by polarization curves, EIS, and immersion tests in m-SBF solution at 37 °C to understand how much corrosion rate can be influenced by the above microstructural difference. Fig. 7 shows the polarization curves of the HPM samples. In polarization curves, the cathodic sides are controlled by hydrogen evolution reaction in aqueous solution, and the other sides are the anodic dissolution reaction, which is dissolution of Mg, and abnormal anodic hydrogen evolution called negative difference effect [40,53]. It is obvious that the cathodic behavior of the three samples is similar. In addition, the anodic sides of all samples have a passivation tendency below the breakdown potential, which implies the presence of oxide films on the surface [54]. The current densities obtained from the polarization curves in the anodic range at +100 mV vs. E_{corr} (before the breakdown potential) for the three samples are 1.8×10^{-5} mA/cm^2 (HPM-R), 1×10^{-4} mA/cm^2 (Mg-C), 2×10^{-5} mA/cm^2 (Mg-A), respectively. This result suggests that the Mg-C with the highest value of current density exhibits the highest anodic dissolution rate [55]. The corrosion potential (E_{corr}) and the corrosion current density (I_{corr}) derived from these curves are shown in Table 3.

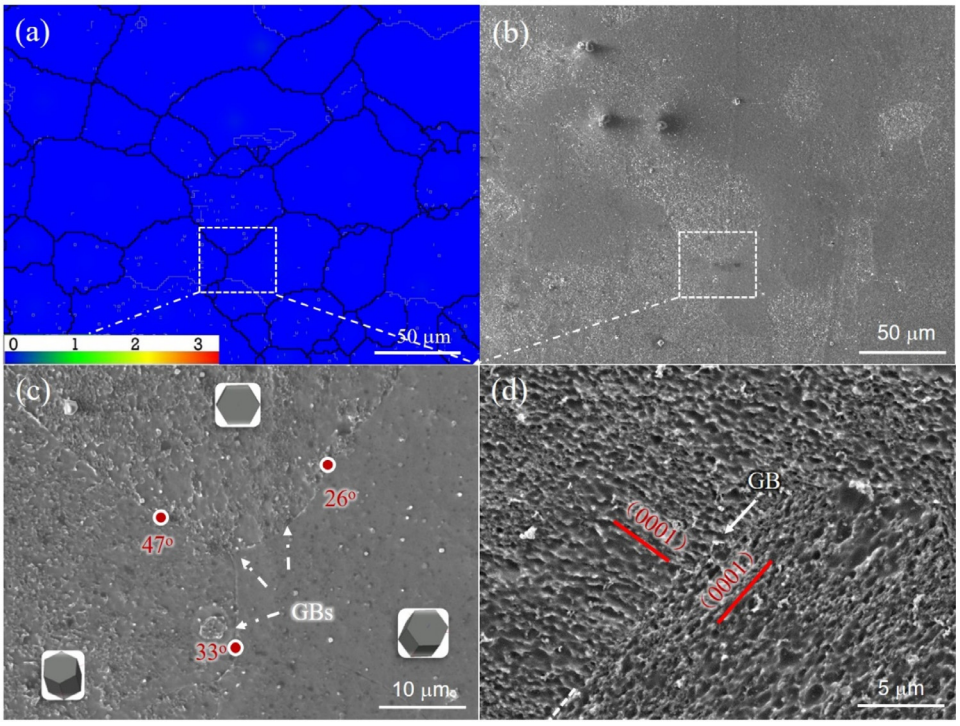

Fig. 5. Local misorientation maps (0°–3°) and corrosion morphology of Mg-A with 30 min immersion in m-SBF at 37 °C. (a) KAM maps of EBSD; (b–d) SEM (Secondary electron mode) images of corrosion morphology without corrosion products (selected high-angle GBs are marked (c)).

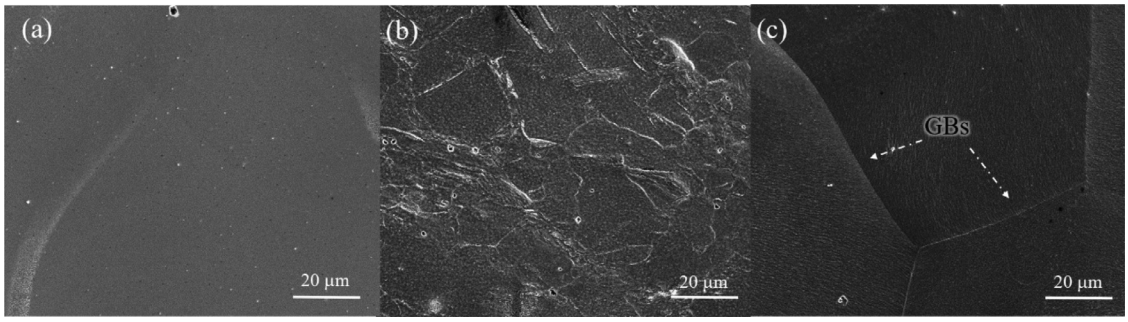

Fig. 6. SEM (secondary electron mode) images of corrosion morphologies without corrosion products of Mg-R (a), Mg-C (b), and Mg-A (c) after 7 days of immersion in m-SBF solution at 37 °C.

Table 3
E_{corr} and I_{corr} values for different HPM samples in m-SBF solution at 37 °C.

Sample	E_{corr} (V vs. Hg/HgCl)	I_{corr} (mA cm^{-2})	-b_c (mV/decade)	b_a (mV/decade)
Mg-R	−1.49 ± 0.03	3.2 ± 0.4 × 10^{-5}	−163	211
Mg-C	−1.49 ± 0.04	7.4 ± 0.7 × 10^{-5}	−171	180
Mg-A	−1.47 ± 0.03	3.8 ± 0.3 × 10^{-5}	−157	224

Fig. 8 shows the EIS spectra of these samples in m-SBF solution after 1 h immersion at 37 °C. The Nyquist spectra of the three samples display a similar electrochemical behavior with a large high-to-medium frequency capacitance loop and one low-frequency capacitance loop. The large capacitive loop is attributed to the charge transfer process of $Mg \rightarrow Mg^{2+}$ at the double layer formed at the surface film [40]. The small capacitive loop is caused by the process in which a corrosion product film is formed on the surface relax [31,56]. The Mg-R and Mg-A have similar impedances, but both loops manifest the Mg-C with the worst corrosion passivity. In the case of Bode plots of Z‘ vs. Frequency as shown in Fig. 8(b), the impedance values always rise from high frequency to low frequency for all samples. Two wave crests can be found in the Bode plots of Phase vs. Frequency, meaning the presence of two capacitance loops.

To further study the corrosion difference of these HPM samples, the equivalent circuit was used to quantitatively analyze the EIS spectra as shown in Fig. 8(a). R_s represents the solution resistance. R_1 and CPE_1 in parallel connection represent the charge transfer resistance and capacitance of electrical double layer at the interface, respectively, which describe the first capacitance loop in high frequency. Normally, the higher charge transfer resistance

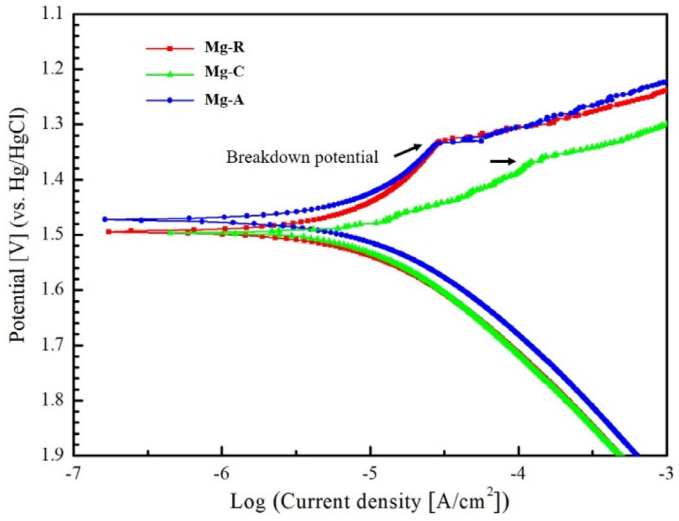

Fig. 7. The potentiodynamic polarization curves of HPM in m-SBF solution at 37 °C.

value implies the lower dissolution rate of the Mg substrate [31]. The constant phase element CPE_1, which represents the capacitive elements associated with nonideal capacitive behavior, is used instead of a capacitor to compensate the nonhomogeneity in the system. CPE impedance is related to the frequency as follows: $Z_{CPE}=1/T(i\omega)^n$, where T is the CPE magnitude and n is the CPE exponent [40,57]. R_2 and C_2 in parallel connection represent the resistance and capacity of the corrosion film, respectively, which are used to describe the second capacitance loop in low frequency. The fitting results by Zview2 software are summarized in Table 4, and the fitted curves are presented in Fig. 8 with solid lines. According to the fitting results, Mg-C has the minimal value of 2021 Ω cm^2 of R_1, implying the highest dissolution rate of the Mg substrate. The values of corrosion film resistance R_2, which is mainly related to the corrosion product formed on the surface in different rolled samples, are in the following order: Mg-R (1838 Ω cm^2) > Mg-A (1358 Ω cm^2) > Mg-C (952 Ω cm^2). Thus, the corrosion product for Mg-R and Mg-A is more protective than that in Mg-C.

The hydrogen evolution method is adopted to study the time-dependent corrosion behavior of Mg [58] as shown in Fig. 9(a). The collected volume of the hydrogen gas, which quantifies the total amount of corrosion at a specific time point, shows a nonlinear relationship with immersion time, suggesting that the corrosion rates of all three samples decrease with time. After 1 week's test, the total hydrogen released increases to 7.8 ± 0.6 ml/cm^2 (Mg-C), 6.3 ± 0.4 ml/cm^2 (Mg-A), and 5.4 ± 0.3 ml/cm^2 (HPM-R). As the amount of hydrogen gas derived from the cathodic reaction is equivalent to the amount of Mg dissolved in the anodic reaction, this observation suggests their corrosion rate also follows the order: Mg-C > Mg-A > HPM-R. Similar results are further confirmed by measuring the mass loss after 1 week of immersion in m-SBF at 37 °C as shown in Fig. 9(b). The average corrosion rates of HPM-R, Mg-C, and Mg-A in a week were 1.10, 1.37, and 1.19 mg/cm^2·day, respectively. By combining with the results of electrochemical test, hydrogen evolution, and mass loss measurement, it can be confirmed that the deformed sample Mg-C with high content of local misorientation has the fastest corrosion rate in m-SBF solution.

4. Discussion

The corrosion rates of HPM show the same following order: Mg-C > Mg-A > HPM-R through different test methods. Mg-R and Mg-C have a similar average grain size and texture, but the corrosion resistance of Mg-C is worse. Thus, we propose that the local misorientation plays a significant role in deteriorating the corrosion resistance of HPM, especially causing GB corrosion. As pure magnesium almost does not contain precipitates, the dislo-

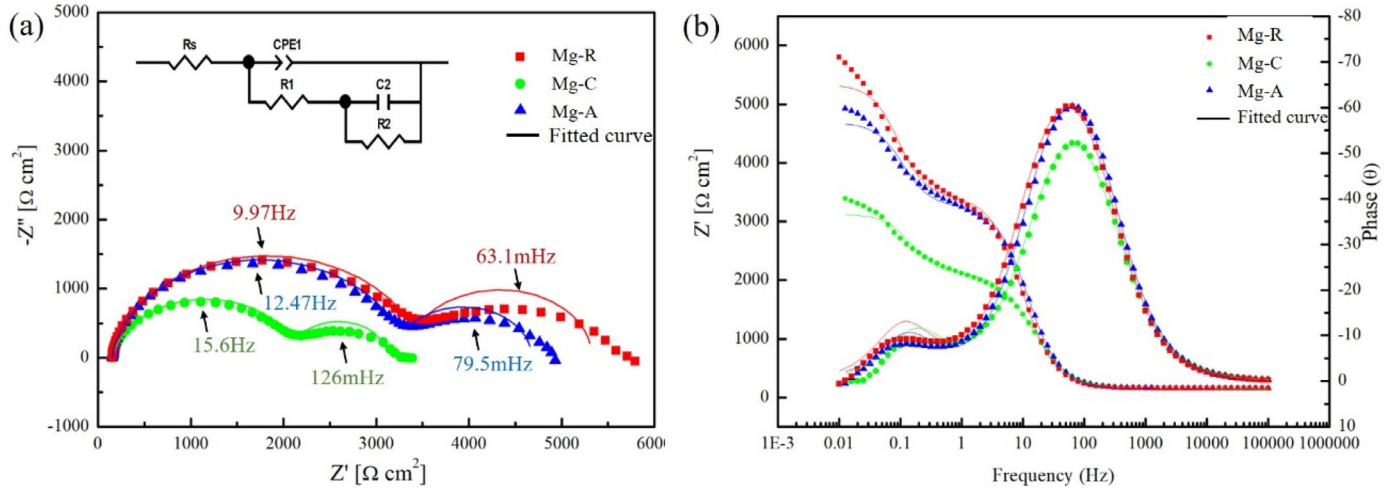

Fig. 8. EIS spectra of HPM with different microstructural factors in m-SBF solution at 37 °C: (a) Nyquist spectral curves; (b) bode plots.

Table 4
Fitting resulting from EIS spectra.

	R_s (Ω cm^2)	CPE_1		R_1 (Ω cm^2)	C_2 (μF cm^{-2})	R_2 (Ω cm^2)	Chi-square
		T_1 (μΩ^{-1} cm^{-2} s^{-1})	n_1				
Mg-R	152 ± 0.8	6.8 ± 0.1	0.92	3339 ± 23	928 ± 43	1838 ± 44	4 × 10^{-3}
Mg-C	150 ± 0.7	9 ± 0.2	0.88	2021 ± 13	1114 ± 51	952 ± 20	4 × 10^{-3}
Mg-A	155 ± 0.6	5.7 ± 0.1	0.93	3166 ± 16	1063 ± 45	1358 ± 29	2 × 10^{-3}

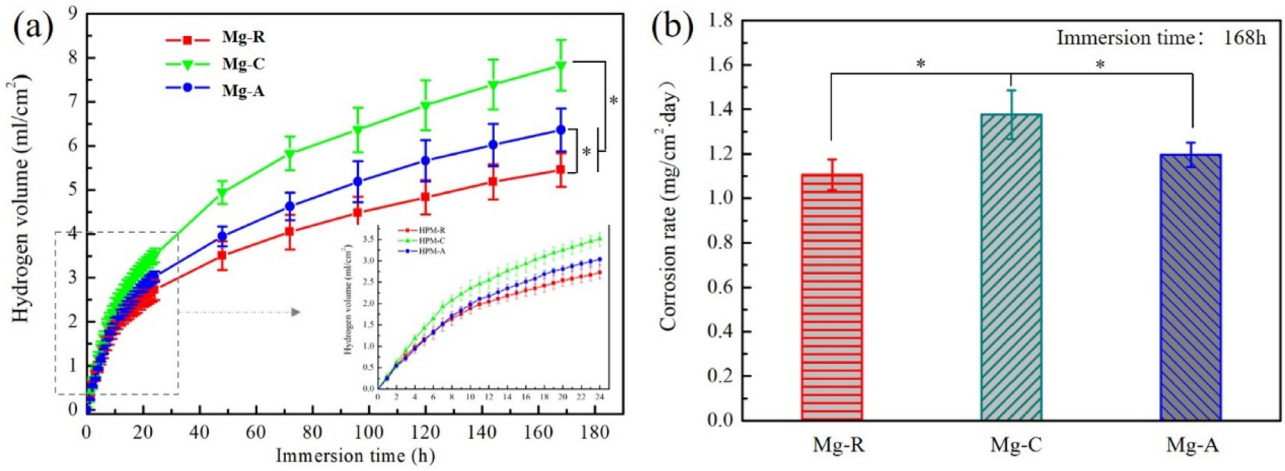

Fig. 9. Representative Mg dissolution estimations of different HPM samples in m-SBF solution at 37 °C: (a) Hydrogen evolution volume as a function of immersion time; (b) Average mass loss rates after 1 week of immersion. $^{*}p < 0.05$.

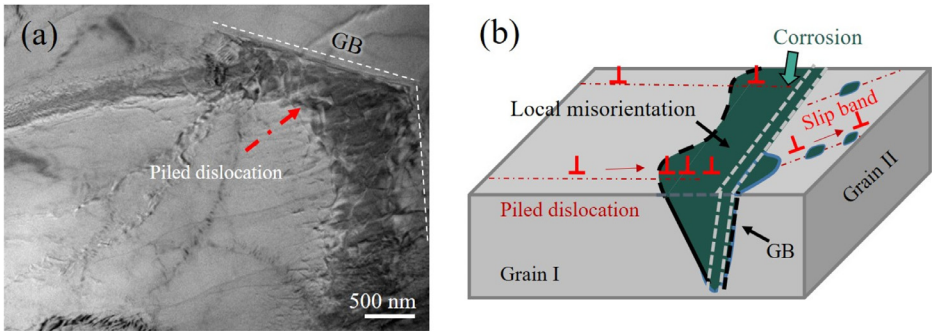

Fig. 10. (a) TEM bright-field image of GBs in Mg-C; (b) a schematic diagram showing corrosion origin at the GB.

cation in the Mg-C sample induced by plastic deformation can move along the slip planes until it meets the GB and eventually piled as shown in the TEM bright-field image of Fig. 10(a). Under this condition, local misorientation within the grain is easily formed. Some dislocations will transform into so-called "extrinsic GB dislocations" [59]. The stress concentration at GB can also activate a new resource of dislocation in the adjacent grain as shown in Fig. 10(b), which may correspond to the corrosion morphology shown in Fig. 4(e). As a net effect, GBs with high densities of such extrinsic GB dislocations would contain increased energy and considerable local misorientation [60]. Therefore, after deformation at room temperature, the regions around GBs with high content of local misorientation are more reactive. This is similar to the result of strain hardening, increasing the corrosion of Mg [45]. In addition, as stated in Zheng's report [34], the corrosion rate of the Mg-Zn alloy increases distinctly after tensile or compressive deformation. The intergranular corrosion is also observed, which provide further certainty for local misorientation-induced GB corrosion of our finding. Thus, at the starting stage of corrosion in Mg-C, the regions around GBs with high local misorientation accompanied by high stored energy and elastic stress are first corroded and then spread along the transverse and longitudinal directions to GB. This characteristic causes corrosion initiating from the GB rather than from the center of the grain as shown in Fig. 10(b). The corrosion product layer during the corrosion origin of Mg-C with immersion 30 min in m-SFB solution was still not homogeneous as shown in Fig. 11(a). On the basis of the segregation of chemical elements including Ca, P, O, and C in the layer of corrosion products as obtained by energy spectrum analysis (Fig. 11(b)–(d)), it could be observed that the layer was porous. When the corrosion propagates, this kind of rough corrosion morphology (Figs. 10(b) and 11(a)) can also increase the contact area of Mg with the corrosive environment, resulting in loss of the stability of the corrosion product layer. From the anodic behavior of polarization curve in Mg-C, the high anodic current density also indicates that the films formed on its surface are less protective than the one formed on the Mg-R and Mg-A. As a comprehensive result, both immersion test and electrochemical testing show that Mg-C has the worst corrosion resistance. The high dissolution rate of the substrate in Mg-C also corresponds to its low charge transfer resistance R_1 value as shown in Fig. 8(a).

The above argument is also supported by the corrosion morphology in Mg-A. The Mg-A corrodes in a homogeneous manner. No obvious corrosion around GBs can be observed after the annealing treatment because lattice defects within grains are recovered with the decrease in local misorientation and even disappear during the annealing process. At the same time, the GB structure recovery consists in bringing GB parameters to normal, which is accompanied by a GB energy decrease [61,62]. Thus, in Mg-A, we cannot observe any local misorientation and local corrosion as shown in Fig. 5(a). The corrosion around GBs is as similar as that in the inner grain as shown in Fig. 5(d). The dissolution rate of the Mg substrate in Mg-A and Mg-R expresses a similar charge transfer resistance R_1 value of EIS spectra as shown in Fig. 8(a) and Table 4 (3126 Ω cm^2 and 3336 Ω cm^2, respectively). Therefore, GB without residual strain is intrinsically nonreactive and less likely

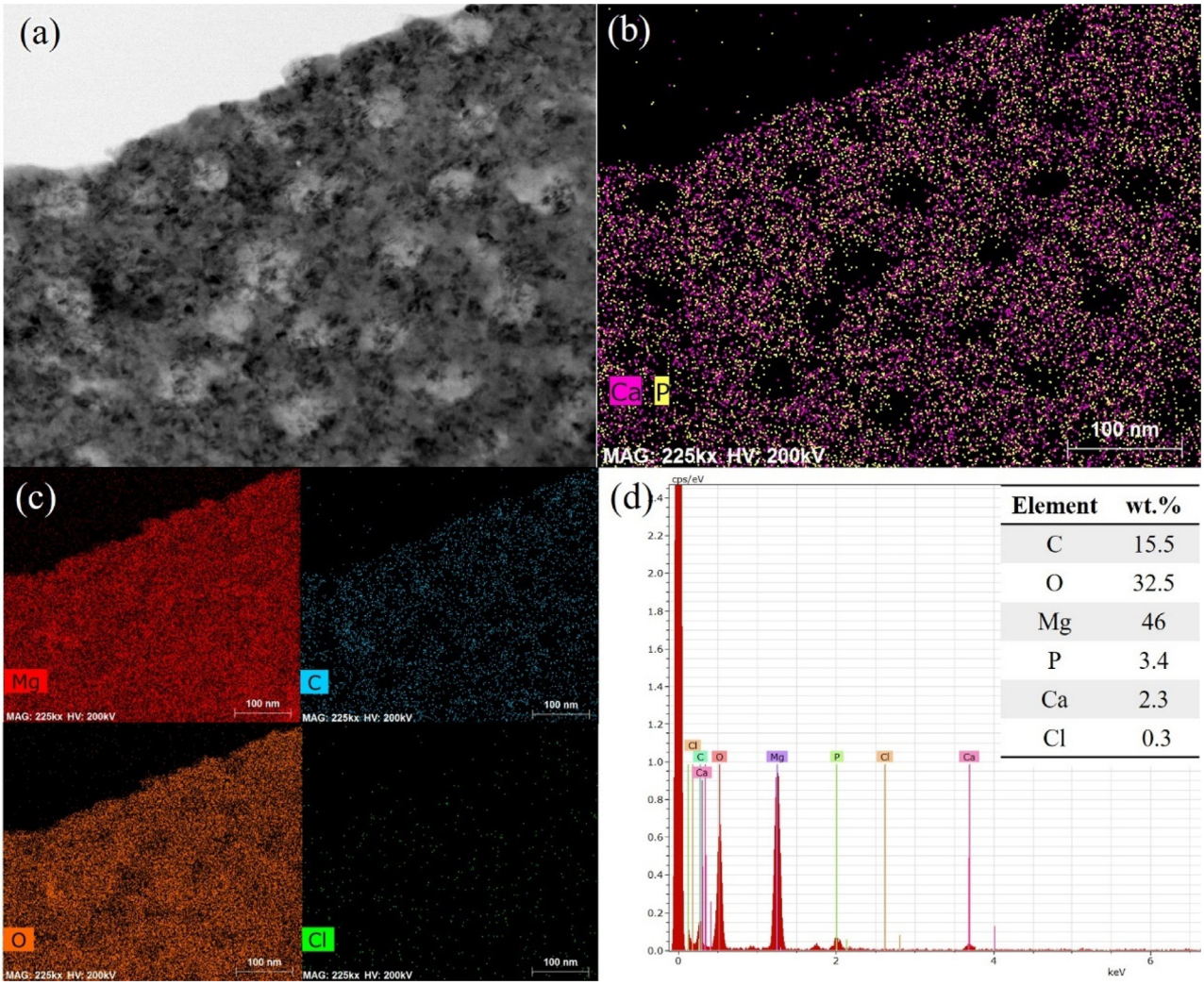

Fig. 11. Bright-field (BF) STEM image of the corroded surface of Mg-C with 30 min immersion in m-SBF solution (a); corresponding EDS elemental maps (b, c) and EDS results (d).

to be an origin of corrosion in HPM. Accordingly, in Song's report [44], grain refinement by ECPE accelerates the corrosion of pure Mg and also causes GB corrosion. With the increase in subsequent annealing time, the corrosion rate can be decreased. For these phenomena, the present study on the local misorientation effect can also give a good explanation.

Except for the effect of local misorientation, it seems that the corrosion rate can be also influenced by grain size (GB density) in our results. Although Mg-R has a little local misorientation and a slight GB corrosion, it has smaller gain size than Mg-A and corrodes more slowly, suggesting the corrosion resistance can be enhanced by refining the grain size. As shown in Fig. 8(a) and Table 4, the value of corrosion film resistance R_2 in Mg-R is evidently higher than that in others, which mainly indicates the corrosion product layer formed on the surface of Mg-R is more protective than that on Mg-A. As suggested in recent studies, refinement of grain size can prove the stability of the corrosion film or enhance their attachment with the Mg substrate [21,23,38,39]. If the fine grains have a weak corrosion resistance, then the possible reason would be that high content of local misorientation is induced during grain refinement. Now, we consider the effect of both local misorientation and GBs during the grain refinement process. The local misorientation can increase corrosion rate as mentioned in our above results and discussion. Grain refinement improving corrosion resistance is based on the mechanism reported by Orlov et al. [38]. We propose a diagram illustrating the possible effects on the whole process of corrosion in three kinds of HPM samples as shown in Fig. 12. For a sample with local misorientation, the corrosion initiates from GB (I in Fig. 12(a)), and the corrosion subsequently propagates into the interior grains through the corroded boundary. For a sample with a little and without local misorientation, a uniform corrosion proceeds until a bilayer structured corrosion products are formed, including a porous outer $Mg(OH)_2$-rich layer on top of an inner MgO-rich layer [63-65] (II and III in Fig. 12(a)). Because of the mismatch in lattice between MgO and $Mg(OH)_2$, an internal stress that is generated between the bilayer structures may lead to a porous, cracked, and less protective corrosion film. For samples with a high GB density, the stress between two corrosion layers is likely relieved from the mismatched GB as shown in Fig. 12(b). Consequently, the sample with less local misorientation and fine grain will have good corrosion resistance. On the basis of the above finding, associating with the clinical application of biomedical Mg, a high local degradation rate could result in the release of a high concentration of degradable products and may also lead to an excessively alkaline environment [18,66]. Moreover, this nonuniform corrosion

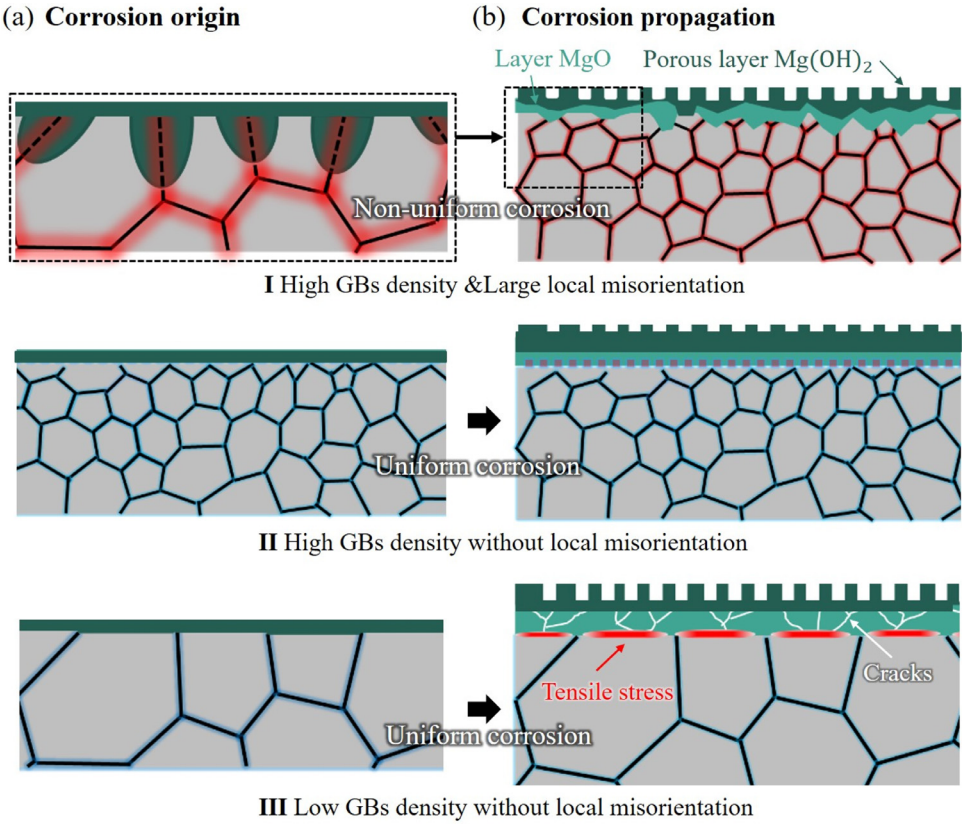

Fig. 12. Schematic diagrams showing the effect of GBs and local misorientation on corrosion origin (a) and corrosion propagation (b).

is likely to cause a stress concentration when the implant is under stress as a structure. Thus, local misorientation can further influence both biological and mechanical performances of biomedical Mg. Therefore, as biodegradable implants, some wrought Mg and its alloys, which are prone to have local misorientation, need attention.

5. Conclusions

In this study, the effect of GB on the corrosion of HPM was examined, and whether the local misorientation accelerates corrosion was investigated systematically by ex situ observation, electrochemistry analysis, and immersion tests. The main conclusions are summarized as follows:

(1) The local misorientation induced by deformation tends to concentrate on the region around GBs and can cause prior corrosion, which leads to GB corrosion and thus deteriorates the corrosion resistance of HPM. After eliminating local misorientation, the corrosion at GB can be diminished. In the annealed HPM, the corrosion activity around GB is similar to that of the inner grain.
(2) In the absence of local misorientation, refining grain size can improve the corrosion resistance of HPM. Therefore, the process of refining grain size and diminishing residual strain offers a promising approach to improve the corrosion resistance of biomedical Mg.

Declaration of Competing Interest

The authors declare that they have no known competing financial interests or personal relationships that could have appeared to influence the work reported in this paper.

Acknowledgments

This work was funded by the National Key R&D Program of China (No. 2018YFC1106600), National Natural Science Foundation of China (NSFC No. 51571142), and the Shanghai Pujiang Program (16PJD034). Wenhui Wang thanks China Scholarship Council (CSC) for the award of fellowship and funding.

Supplementary materials

Supplementary material associated with this article can be found, in the online version, at doi:10.1016/j.actbio.2019.10.036.

References

[1] Y.F. Zheng, X.N. Gu, F. Witte, Biodegradable metals, Mater. Sci. Eng. R: Rep. 77 (2014) 1–34.
[2] H. Yang, C. Wang, C. Liu, H. Chen, Y. Wu, J. Han, Z. Jia, W. Lin, D. Zhang, W. Li, W. Yuan, H. Guo, H. Li, G. Yang, D. Kong, D. Zhu, K. Takashima, L. Ruan, J. Nie, X. Li, Y. Zheng, Evolution of the degradation mechanism of pure zinc stent in the one-year study of rabbit abdominal aorta model, Biomaterials 145 (2017) 92–105.
[3] C. Shuai, Y. Cheng, Y. Yang, S. Peng, W. Yang, F. Qi, Laser additive manufacturing of Zn–2Al part for bone repair formability, microstructure and properties, J. Alloys Compd. 798 (2019) 606–615.
[4] C. Gao, M. Yao, S. Li, P. Feng, S. Peng, C. Shuai, Highly biodegradable and bioactive Fe-Pd-bredigite biocomposites prepared by selective laser melting, J. Adv. Res. 20 (2019) 91–104.
[5] C. Shuai, B. Wang, Y. Yang, S. Peng, C. Gao, 3D honeycomb nanostructure-encapsulated magnesium alloys with superior corrosion resistance and mechanical properties, Compos. Part B 162 (2019) 611–620.
[6] X. Liu, J. Sun, F. Zhou, Y. Yang, R. Chang, K. Qiu, Z. Pu, L. Li, Y. Zheng, Micro-alloying with Mn in Zn–Mg alloy for future biodegradable metals application, Mater. Des. 94 (2016) 95–104.
[7] L. Ren, K. Yang, Bio-functional design for metal implants, a new concept for development of metallic biomaterials, J. Mater. Sci. Technol. 29 (2013) 1005–1010.
[8] Y. Zhang, J. Xu, Y.C. Ruan, M.K. Yu, M. O'Laughlin, H. Wise, D. Chen, L. Tian, D. Shi, J. Wang, S. Chen, J.Q. Feng, D.H. Chow, X. Xie, L. Zheng, L. Huang, S. Huang, K. Leung, N. Lu, L. Zhao, H. Li, D. Zhao, X. Guo, K. Chan, F. Witte,

H.C. Chan, Y. Zheng, L. Qin, Implant-derived magnesium induces local neuronal production of CGRP to improve bone-fracture healing in rats, Nat. Med. 22 (2016) 1160–1169.
[9] X. Gu, Y. Zheng, Y. Cheng, S. Zhong, T. Xi, In vitro corrosion and biocompatibility of binary magnesium alloys, Biomaterials 30 (2009) 484–498.
[10] S. Zhang, X. Zhang, C. Zhao, J. Li, Y. Song, C. Xie, H. Tao, Y. Zhang, Y. He, Y. Jiang, Y. Bian, Research on an Mg-Zn alloy as a degradable biomaterial, Acta Biomater. 6 (2010) 626–640.
[11] Y. Yang, X. Guo, C. He, C. Gao, C. Shuai, Regulating degradation behavior by incorporating mesoporous silica for mg bone implants, ACS Biomater. Sci. Eng. 4 (2018) 1046–1054.
[12] X. Zhang, H. Zu, D. Zhao, K. Yang, S. Tian, X. Yu, F. Lu, B. Liu, X. Yu, B. Wang, W. Wang, S. Huang, Y. Wang, Z. Wang, Z. Zhang, Ion channel functional protein kinase TRPM7 regulates Mg ions to promote the osteoinduction of human osteoblast via PI3K pathway: in vitro simulation of the bone-repairing effect of Mg-based alloy implant, Acta Biomater. 63 (2017) 369–382.
[13] P. Cheng, P. Han, C. Zhao, S. Zhang, H. Wu, J. Ni, P. Hou, Y. Zhang, J. Liu, H. Xu, S. Liu, X. Zhang, Y. Zheng, Y. Chai, High-purity magnesium interference screws promote fibrocartilaginous entheses regeneration in the anterior cruciate ligament reconstruction rabbit model via accumulation of BMP-2 and VEGF, Biomaterials 81 (2016) 14–26.
[14] P. Han, P. Cheng, S. Zhang, C. Zhao, J. Ni, Y. Zhang, W. Zhong, P. Hou, X. Zhang, Y. Zheng, Y. Chai, In vitro and in vivo studies on the degradation of high-purity Mg (99.99 wt.%) screw with femoral intracondylar fractured rabbit model, Biomaterials 64 (2015) 57–69.
[15] Y. Yua, H. Lu, J. Suna, Long-term in vivo evolution of high-purity Mg screw degradation-local and systemic effects of Mg degradation products, Acta Biomater. 71 (2018) 215–244.
[16] F. Witte, The history of biodegradable magnesium implants: a review, Acta Biomater. 6 (2010) 1680–1692.
[17] J. Chen, L. Tan, K. Yang, Recent advances on the development of biodegradable magnesium alloys: a review, Mater. Technol. 31 (2016) 681–688.
[18] D. Zhao, F. Witte, F. Lu, J. Wang, J. Li, L. Qin, Current status on clinical applications of magnesium-based orthopaedic implants: a review from clinical translational perspective, Biomaterials 112 (2017) 287–302.
[19] A.H. Martinez Sanchez, B.J. Luthringer, F. Feyerabend, R. Willumeit, Mg and Mg alloys: how comparable are in vitro and in vivo corrosion rates? A review, Acta Biomater. 13 (2015) 16–31.
[20] M. Esmaily, J.E. Svensson, S. Fajardo, N. Birbilis, G.S. Frankel, S. Virtanen, R. Arrabal, S. Thomas, L.G. Johansson, Fundamentals and advances in magnesium alloy corrosion, Prog. Mater. Sci. 89 (2017) 92–193.
[21] Z. Pu, G.L. Song, S. Yang, J.C. Outeiro, O.W. Dillon, D.A. Puleo, I.S. Jawahir, Grain refined and basal textured surface produced by burnishing for improved corrosion performance of AZ31B Mg alloy, Corros. Sci. 57 (2012) 192–201.
[22] S. Gollapudi, Grain size distribution effects on the corrosion behaviour of materials, Corros. Sci. 62 (2012) 90–94.
[23] N. Birbilis, K.D. Ralston, S. Virtanen, H.L. Fraser, C.H.J. Davies, Grain character influences on corrosion of ECAPed pure magnesium, Corros. Eng. Sci. Technol. 45 (2013) 224–230.
[24] Y. Song, E.-.H. Han, D. Shan, C.D. Yim, B.S. You, The role of second phases in the corrosion behavior of Mg-5 Zn alloy, Corros. Sci. 60 (2012) 238–245.
[25] Y. Song, E.-.H. Han, K. Dong, D. Shan, C.D. Yim, B.S. You, Study of the corrosion product films formed on the surface of Mg–xZn alloys in NaCl solution, Corros. Sci. 88 (2014) 215–225.
[26] J. Li, Q. Jiang, H. Sun, Y. Li, Effect of heat treatment on corrosion behavior of AZ63 magnesium alloy in 3.5 wt.% sodium chloride solution, Corros. Sci. 111 (2016) 288–301.
[27] B. Wang, D. Xu, J. Dong, W. Ke, Effect of texture on biodegradable behavior of an as-extruded Mg–3%Al–1%Zn alloy in phosphate buffer saline medium, J. Mater. Sci. Technol. 32 (2016) 646–652.
[28] G.-.L. Song, The effect of texture on the corrosion behavior of AZ31 Mg alloy, JOM 64 (2012) 671–679.
[29] B.J. Wang, D.K. Xu, J.H. Dong, W. Ke, Effect of the crystallographic orientation and twinning on the corrosion resistance of an as-extruded Mg–3Al–1Zn (wt.%) bar, Scr. Mater. 88 (2014) 5–8.
[30] S. Pawar, T.J.A. Slater, T.L. Burnett, X. Zhou, G.M. Scamans, Z. Fan, G.E. Thompson, P.J. Withers, Crystallographic effects on the corrosion of twin roll cast AZ31 Mg alloy sheet, Acta Mater. 133 (2017) 90–99.
[31] Y. Song, E.-.H. Han, D. Shan, C.D. Yim, B.S. You, The effect of Zn concentration on the corrosion behavior of Mg–xZn alloys, Corros. Sci. 65 (2012) 322–330.
[32] H. Miao, H. Huang, Y. Shi, H. Zhang, J. Pei, G. Yuan, Effects of solution treatment before extrusion on the microstructure, mechanical properties and corrosion of Mg-Zn-Gd alloy in vitro, Corros. Sci. 122 (2017) 90–99.
[33] C. Shuai, Y. Zhou, Y. Yang, C. Gao, S. Peng, G. Wang, Ag-introduced antibacterial ability and corrosion resistance for bio-mg alloys, Biomed. Res. Int. 2018 (2018) 13.
[34] Y. Zheng, Y. Li, J. Chen, Z. Zou, Effects of tensile and compressive deformation on corrosion behaviour of a Mg–Zn alloy, Corros. Sci. 90 (2015) 445–450.
[35] J. Hu, Y.N. Shi, X. Sauvge, G. Sha, K. Lu, Grain boundary stability governs hardening and softening in extremely fine nanograined metals, Science 355 (2017) 1292–1296.
[36] R.Z. Valiev, Nanostructuring of metals by severe plastic deformation for advanced properties, Nat. Mater. 3 (2004) 511–516.
[37] K.D. Ralston, N. Birbilis, C.H.J. Davies, Revealing the relationship between grain size and corrosion rate of metals, Scr. Mater. 63 (2010) 1201–1204.
[38] D. Orlov, K.D. Ralston, N. Birbilis, Y. Estrin, Enhanced corrosion resistance of Mg alloy ZK60 after processing by integrated extrusion and equal channel angular pressing, Acta Mater. 59 (2011) 6176–6186.
[39] J. Liao, M. Hotta, N. Yamamoto, Corrosion behavior of fine-grained AZ31B magnesium alloy, Corros. Sci. 61 (2012) 208–214.
[40] Q. Liu, Q.-x. Ma, G.-q. Chen, X. Cao, S. Zhang, J.-l. Pan, G. Zhang, Q.-y. Shi, Enhanced corrosion resistance of AZ91 magnesium alloy through refinement and homogenization of surface microstructure by friction stir processing, Corros. Sci. 138 (2018) 284–296.
[41] K.D. Ralston, B. Nick, Effect of grain size on corrosion a review, Corrosion 66 (2010) 075005.
[42] P. Minarik, E. Jablonska, R. Kral, J. Lipov, T. Ruml, C. Blawert, B. Hadzima, F. Chmelik, Effect of equal channel angular pressing on in vitro degradation of LAE442 magnesium alloy, Mater. Sci. Eng. C, Mater. Biol. Appl. 73 (2017) 736–742.
[43] D. Song, A.B. Ma, J.H. Jiang, P.H. Lin, D.H. Yang, J.F. Fan, Corrosion behaviour of bulk ultra-fine grained AZ91D magnesium alloy fabricated by equal-channel angular pressing, Corros. Sci. 53 (2011) 362–373.
[44] D. Song, A. Ma, J. Jiang, P. Lin, D. Yang, J. Fan, Corrosion behavior of equal-channel-angular-pressed pure magnesium in NaCl aqueous solution, Corros. Sci. 52 (2010) 481–490.
[45] Y. Snir, G. Ben-Hamu, D. Eliezer, E. Abramov, Effect of compression deformation on the microstructure and corrosion behavior of magnesium alloys, J. Alloys Compd. 528 (2012) 84–90.
[46] S.I. Wright, M.M. Nowell, D.P. Field, A review of strain analysis using electron backscatter diffraction, Microsc. Microanal. 17 (2011).
[47] R. Jasionowski, D. Zasada, W. Polkowski, EBSD strain analysis of CuZn10 cast alloy during cavitational wear, Arch. Foundry Eng. 13 (2013) 51–56.
[48] A. Oyane, H.-M. Kim, T. Furuya, T. Kokubo, T. Miyazaki, T. Nakamura, Preparation and assessment of revised simulated body fluids, J. Biomed. Mater. Res. 65A (2003) 188–195.
[49] X.C. Liu, H.W. Zhang, K. Lu, Strain-induced ultrahard and ultrastable nanolaminated structure in nickel, Science 342 (2013) 337–340.
[50] R. Zhang, Y. Qiu, Y. Qi, N. Birbilis, A closer inspection of a grain boundary immune to intergranular corrosion in a sensitised Al-Mg alloy, Corros. Sci. 133 (2018) 1–5.
[51] K. Hagihara, M. Okubo, M. Yamasaki, T. Nakano, Crystal-orientation-dependent corrosion behaviour of single crystals of a pure Mg and Mg-Al and Mg-Cu solid solutions, Corros. Sci. 109 (2016) 68–85.
[52] K.S. Shin, M.Z. Bian, N.D. Nam, Effects of crystallographic orientation on corrosion behavior of magnesium single crystals, JOM 64 (2012) 664–670.
[53] G.L. Song, A. Atrens, Corrosion mechanisms of magnesium alloys, Adv. Eng. Mater. 1 (1999) 11–33.
[54] F. Cao, G.-.L. Song, A. Atrens, Corrosion and passivation of magnesium alloys, Corros. Sci. 111 (2016) 835–845.
[55] S. Leleu, B. Rives, N. Causse, N. Pébère, Corrosion rate determination of rare-earth Mg alloys in a Na_2 SO_4 solution by electrochemical measurements and inductive coupled plasma-optical emission spectroscopy, J. Magnes. Alloys 7 (2019) 47–57.
[56] P.L. Bonora, M. Andrei, A. Eliezer, E.M. Gutman, Corrosion behaviour of stressed magnesium alloy, Corros. Sci. 44 (2002) 729–749.
[57] R. Arrabal, A. Pardo, M.C. Merino, M. Mohedano, K. Paucar, G. Garcés, Effect of Nd on the corrosion behaviour of AM50 and AZ91D magnesium alloys in 3.5 wt.% NaCl solution, Corros. Sci. 55 (2012) 301–312.
[58] G.L. Song, A. Atrens, Understanding magnesium corrosion—a framework for improved alloy performance, Adv. Eng. Mater. 5 (2003) 837–858.
[59] A.A. Nazarov, A.E. Romanov, R.Z. Valiev, On the structure, stress fields and energy of nonequilibrium grain boundaries, Acta Metall. 14 (1993) 1033–1040.
[60] X. Sauvage, G. Wilde, S.V. Divinski, Z. Horita, R.Z. Valiev, Grain boundaries in ultrafine grained materials processed by severe plastic, Mater. Sci. Eng. A 540 (2012) 1–12.
[61] R.Z. Valiev, V.Y. Gertsman, O.A. Kaibyshev, On the nature of grain boundary structure recovery, Phys. Status Solidi (A) 61 (1980) 95–99.
[62] R.Z. Valiev, V.Y. Gertsman, O.A. Kaibyshev, Grain boundary structure and properties under external influences, Phys. Status Solidi (A) 97 (1986) 11–56.
[63] M. Taheri, R.C. Phillips, J.R. Kish, G.A. Botton, Analysis of the surface film formed on Mg by exposure to water using a FIB cross-section and STEM–EDS, Corros. Sci. 59 (2012) 222–228.
[64] M. Taheri, M. Danaie, J.R. Kish, TEM examination of the film formed on corroding mg prior to breakdown, J. Electrochem. Soc. 161 (2013) C89–C94.
[65] M.P. Brady, G. Rother, L.M. Anovitz, K.C. Littrell, K.A. Unocic, H.H. Elsentriecy, G.L. Song, J.K. Thomson, N.C. Gallego, B. Davis, Film breakdown and nano–porous Mg(OH)2 formation from corrosion of magnesium alloys in salt solutions, J. Electrochem. Soc. 162 (2015) C140–C149.
[66] J. Wang, F. Witte, T. Xi, Y. Zheng, K. Yang, Y. Yang, D. Zhaog, J. Meng, Y. Li, W. Li, K. Chan, L. Qin, Recommendation for modifying current cytotoxicity testing standards for biodegradable magnesium-based materials, Acta Biomater. 21 (2015) 237–249.